Energy Storage Materials 37 (2021) 509–520

Contents lists available at ScienceDirect

Energy Storage Materials

journal homepage: www.elsevier.com/locate/ensm

Tailoring bulk Li^+ ion diffusion kinetics and surface lattice oxygen activity for high-performance lithium-rich manganese-based layered oxides

Ruizhi Yu[a,b], Mohammad Norouzi Banis[b], Changhong Wang[b,d], Bing Wu[a], Yan Huang[a], Shuang Cao[a], Junjie Li[b], Sidra Jamil[a], Xiaoting Lin[b], Feipeng Zhao[b], Wenhuai Lin[a], Baobao Chang[c], Xiukang Yang[a], Huan Huang[d], Xianyou Wang[a,*], Xueliang Sun[b,**]

[a] National Local Joint Engineering Laboratory for Key Materials of New Energy Storage Battery, National Base for International Science & Technology Cooperation, Hunan Province Key Laboratory of Electrochemical Energy Storage & Conversion, School of Chemistry, Xiangtan University, Xiangtan, Hunan, 411105, China
[b] Department of Mechanical and Materials Engineering, University of Western Ontario, London, Ontario, N6A 5B9, Canada
[c] Key laboratory of Materials Processing and Mold of Ministry of Education, Zhengzhou University, Zhengzhou, Henan, 450001, China
[d] Glabat Solid-State Battery Inc., 700 Collip Circle, London, Ontario, N6G 4X8, Canada

ARTICLE INFO

Keywords:
Lithium-ion batteries
Lithium-rich manganese-based layered oxides
Doping
Cationic and anionic redox activity
Surface lattice oxygen

ABSTRACT

Lithium-rich manganese-based layered oxides (LRMOs) offer joint cationic and anionic redox at a high voltage, thus promising high energy density for lithium-ion batteries (LIBs). However, the restive anion redox is also connected with poor rate performance, severe capacity fading, and continuous voltage decay. Herein, a successful strategy for enhancing the Li^+ ion diffusivity and structure stability of LRMOs is proposed. The obtained material possesses high cationic and anionic redox activity due to the introduction of Te^{6+}. Moreover, a heterogeneous protective layer that is composed of acid-resistant $Mg_3(PO_4)_2$ and self-induced cation-disordered phase with passivated lattice oxygen is verified to be located on the surface of the material, thereby restraining the structural degeneration. Benefitting from the unique architecture, the modified material presents a favorable cycling performance and excellent rate capability (178.8 mA h g^{-1}, 10 C). More importantly, the voltage decay is significantly suppressed during cycling. The finding here exhibits the importance of activating cationic and anionic redox in the bulk and passivating surface oxygen for enhancing reversible capacity at high rates and improving structural stability, providing a ponderable way to promote the electrochemical performance of LRMOs.

1. Introduction

Lithium-rich manganese-based layered oxides (LRMOs) with the composition of $xLi_2MnO_3 \bullet (1\text{-}x)LiTMO_2$ (TM = Mn, Ni, Co, etc.) have been perceived as the potential next-generation cathode materials for the high-performance lithium-ion batteries (LIBs) owing to the extraordinarily high specific capacity (exceeding 250 mA h g^{-1}, 2.0-4.6 V vs Li/Li^+), comparatively high average discharge voltage (exceeding 3.5 V vs Li/Li^+) and reduced cost [1-4]. Based on the first-principle calculations and experimental work, the extremely high capacity resulted from LRMOs can be ascribed to the combined contributions of both the cationic redox couple of transition-metal ions ($TM^{n+}/TM^{(n+1)+}$) and the anionic redox couple of oxygen species (O^{2-}/O^{n-}) [5-9]. In spite of furnishing high capacity, the unique reaction mechanism, especially the indisciplinable oxygen redox, triggers some issues. For instance, the lattice oxygen is easily oxidized to oxygen gas on the surface of particles and accompanied by some irreversible Li^+ ions extraction from the lattice at the high voltage of > 4.5 V. This process is always in conjunction with possible electrolyte decomposition at the high voltage, resulting in a large initial irreversible capacity and safety issues [7,9]. Recently, Bruce's group [5] presented that O_2 formed during initial charge plateau (> 4.5 V) in the honeycomb-ordered TM layer can be trapped in vacancy cluster defects within the bulk of particles due to the in-plane TM ions migration into the vacated Li^+ sites. Though the O_2 can be reduced on discharge to O^{2-}, the honeycomb superstructure cannot be recovered as it was rapidly repopulated by Li^+ ions, which can block TM ions migration. This irreversible structural rearrangement changed the coordination environment around O from two TM ions and one Li^+ ion to only

* Corresponding author at: National Local Joint Engineering Laboratory for Key Materials of New Energy Storage Battery, National Base for International Science & Technology Cooperation, Hunan Province Key Laboratory of Electrochemical Energy Storage & Conversion, School of Chemistry, Xiangtan University, Xiangtan, Hunan, 411105, China.
** Co-Corresponding author at: Department of Mechanical and Materials Engineering, University of Western Ontario, London, Ontario, N6A 5B9, Canada.
E-mail addresses: wxianyou@yahoo.com (X. Wang), xsun9@uwo.ca (X. Sun).

https://doi.org/10.1016/j.ensm.2021.02.025
Received 9 September 2020; Received in revised form 24 January 2021; Accepted 15 February 2021
Available online 17 February 2021

Li^+ ions, boosting the energy level of the O 2p states and leading to a lower voltage on discharge compared with charge, which can cause voltage hysteresis. Moreover, numerous investigations have demonstrated that the anion redox during cycling was coupled with irreversible loss of lattice oxygen and cation migration on continuous cycling [6,10-14], which can induce irreversible structural transformation from layered to deficient spinel-like [3,5,14-18]. These processes involve the Li^+ ions and oxygen release from the lattice, which can generate structural strain and result in lattice breakdown and particle fracture. Thus, the oxygen loss and phase transformation have proved to be a major factor of the continuous voltage and capacity fading [11,19,20]. Furthermore, Tarascon's group [6] has pointed out that the anion redox in the LRMOs exhibited sluggish charge-transfer and diffusion kinetics, which was disadvantageous for fast charge/discharge cycling. In brief, the low initial coulombic efficiency, severe voltage hysteresis and decay, successive capacity fading, and inferior rate capability lead to severe restrictions for the commercialization of LRMOs.

Because various side reactions occur at the electrode/electrolyte interface, surface modification can be an effective route for mitigating the capacity decline by preventing the host materials from erosion by acidic species in the electrolyte [21-25]. Song et al. [23] reported an in-situ dispersion method to construct a nano-$AlPO_4$ coating layer on the surface of LRMOs and a capacity retention of 90% after 100 cycles can be obtained for the $AlPO_4$ coated $Li_{1.15}Ni_{0.17}Co_{0.11}Mn_{0.57}O_2$ materials. Zhao et al. [24] synthesized high-performance Er_2O_3-coated LRMOs, which illustrated significantly enhanced cycling performance with an ultrahigh capacity retention of 101% after 300 cycles. Though the surface coating works quite well in enhancing cycling performance, the overall effectiveness against voltage fading remains unsatisfactory. In addition, the improvement of rate capability is inconspicuous for the coated LRMOs due to the unaltered low diffusivity of Li^+ ions in the bulk. Cation and anion doping were proposed to improve the cycling stability and impede the voltage fading by alleviating the TM migration in LRMOs [19,20,26-30]. For example, Sallard et al. substituted partial Li of LRMOs with Mg and reported that Mg substitution could hinder the TM migration from TM slabs to Li layers during cycling due to the strong coulombic repulsion between Mg^{2+} and Mn^{n+}, thus restraining the structural transformation. The Mg-doped cathode materials delivered a mitigated voltage fading rate of ~0.80 mV per cycle as compared to a voltage fading rate of ~1.31 mV per cycle for the pristine material [26]. Nevertheless, doping usually results in lowering the specific capacity because of the incorporation of inactive dopants.

Recently, some researchers found that a minority of coating layer and dopant can affect the phase structure and the lattice oxygen activity of LRMOs, thus enhancing the electrochemical properties [31-35]. Zhu et al. [32] reported that surface treatment of LRMOs using a molten-molybdate leaching method could induce a crystal-dense $LiMn_{1.5}Ni_{0.5}O_4$ shell in the surface region of LRMOs, this anion-redox-free shell can prevent global oxygen migration during cycling, thus mitigating oxygen release and phase collapse. The mitigated global oxygen migration (GOM) was conducive to enhancing the initial coulombic efficiency and maintaining the high discharge voltage platform. Zhao et al. [33] presented a heterostructured $LiAlF_4$ coating method to obtain a high proportion of oxidized nonbonding O^{n-} species in the LRMOs, which can significantly increase the anionic redox kinetics. As a result, the LRMOs@$LiAlF_4$ electrodes exhibited outstanding rate capability (133 mA h g^{-1}, 5 C). In our previous work [34], Sb was doped into the TM site and the results demonstrated that Sb could donate extra electrons to O and alleviate the excessive O participation of charge compensation, which can stabilize lattice oxygen structure. The Sb-doped LRMOs illustrated high cycling performance with a capacity retention of 86.9% after 200 cycles at 1 C and suppressed voltage fading. However, the specific capacity of the Sb-doped LRMOs was a little lower than the pristine LRMOs due to the decreased activity of lattice oxygen. Wang's group [35] addressed the capacity and voltage fading by surface doping of heavy ions (Nb, Ti, and Zr) in the LRMOs. It can be found that the strong Nb-O, Ti-O, and Zr-O bonding integrated the surface structure and passivated the surface lattice oxygen but didn't influence the bulk lattice oxygen of the LRMOs. The modified cathode materials obtained a high initial reversible capacity of 320 mA h g^{-1} at 0.1 C with high coulombic efficiency of 87% and excellent cycling performance with a capacity retention of 94.5% after 100 cycles. Moreover, the average discharge voltage drops only by 136 mV during cycling. Thus, tuning the phase structure and electronic structure of bulk and surface lattice oxygen is crucial to stabilizing the high energy and power density of LRMOs.

Overall, in light of the unique electrochemical reaction mechanism of LRMOs and the tremendous efforts on the modification of these materials with coating and doping, some concerns need still to be addressed to enhance their electrochemical performance: (1) cationic/anionic redox activity and Li^+ ion diffusion rates should be enhanced through bulk doping to obtain high rate capability; (2) the coating layer should be electrochemically inert and completed to avoid the side reaction between the LRMOs and electrolyte; (3) the surface layered structure should be induced to be a more stable phase and/or the surface lattice oxygen should be passivated to suppress the oxygen release and phase transformation from surface to bulk.

The non-transition metal ions with the completely filled (or no) d-orbitals were reported to induce a formation of less directional M-O bond, which can change the local environment around lattice oxygen, prompting the formation of peroxo-like species, and improve anionic redox activity in Li-excess materials during cycling [33,36]. Furthermore, it is noteworthy that the valences of Ni, Co, and Mn are +2, +3, and +4 in the LRMOs, separately [34,37]. Thus, doping the LRMOs with high valence (> +4) ions can decrease the average valence of TM ions in LRMOs and enhance the cationic redox activity [38]. As a result, Te^{6+} ions with completely filled d-orbitals and high valence (+6) can meet the qualifications as the appropriate dopants. Besides, to avoid the direct contact between the high active bulk and electrolyte, $Mg_3(PO_4)_2$ was coated on the surface of Te^{6+}-doped LRMOs. Because the stable P=O bonds in $Mg_3(PO_4)_2$ can provide high ionic conductivity and withstand the erosion of acidic species [23,39,40]. Moreover, a cation-disordered phase with less Li-O-Li configuration than the conventional well-ordered structure was introduced between the bulk layered structure and coating layer, which can greatly decrease the surface lattice oxygen activity [12]. Thus, a suppressed phase transformation from the surface to bulk can be obtained in this regard. Taking advantage of Te^{6+} dopant and heterogeneous protective layer, the new LRMOs can deliver outstanding electrochemical properties including high reversible capacity, slight voltage fading, and excellent rate capability, as schematically illustrated in **Fig. 1**. Although intensive works on surface coating and doping have been previously explored, it is important to emphasize that this work provides significant design guidance for the industrialization of LRMOs with practically high specific power and energy.

2. Experimental section

2.1. Material preparation

A pristine lithium-rich manganese-based layered cathode material $Li_{1.4}Mn_{0.6}Ni_{0.2}Co_{0.2}O_{2+x}$ (LMNCO-P) was synthesized by a two-step process containing co-precipitation followed by high-temperature calcination. Firstly, a 1.6 mol L^{-1} mixed aqueous solution of $MnSO_4 \bullet H_2O$, $NiSO_4 \bullet 6H_2O$ and $CoSO_4 \bullet 7H_2O$ (Mn : Ni : Co = 3 : 1 : 1, molar ratio), 1.6 mol L^{-1} aqueous solution of Na_2CO_3 and desired amount of $NH_3 \bullet H_2O$ solution were prepared, separately. Then, the as-prepared solutions were pumped into a reaction tank at a proper flow rate. The pH value and the temperature of the suspension in the reaction tank were adjusted at 7.5 and 55 °C. After stirring for 15 h, the as-prepared carbonate precursor $Mn_{0.6}Ni_{0.2}Co_{0.2}CO_3$ was washed with deionized water several times and then vacuum dried at 110 °C for 12 h. Subsequently, the precursor was converted into oxide powder by calcining at 500 °C for 6 h. After that,

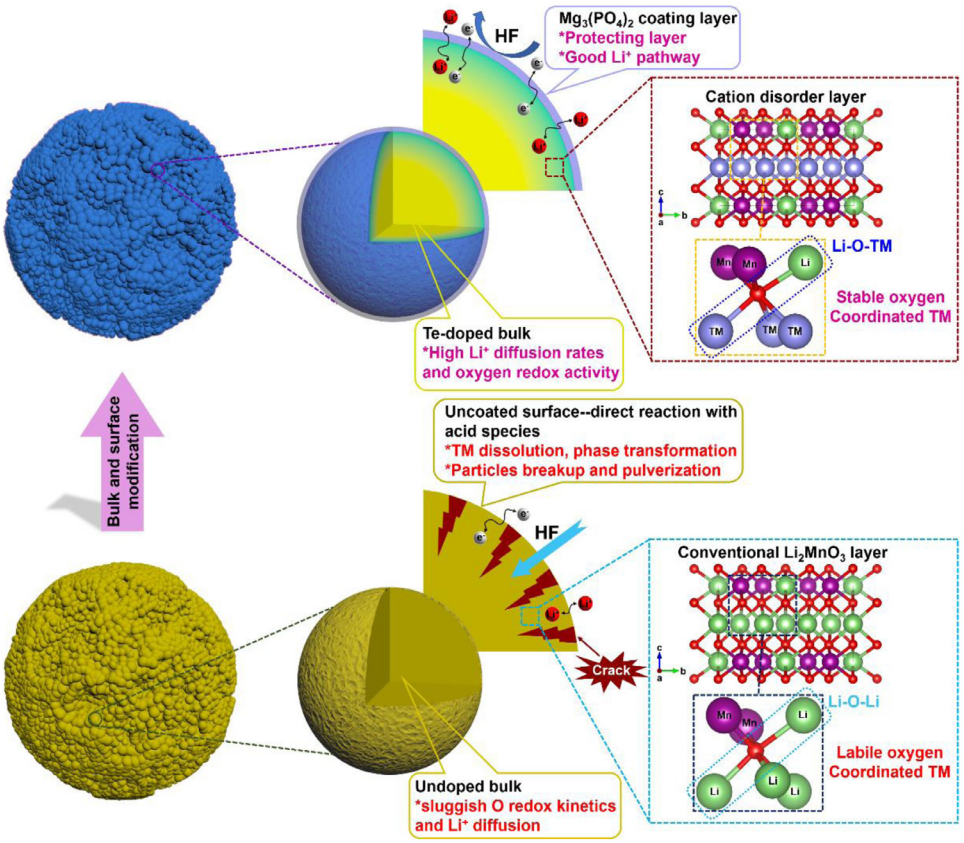

Fig. 1. Schematic diagram of design strategy of the Te-doped lithium-rich manganese-based layered oxides with a heterogeneous protective layer.

the oxide powder was fully ground with a desired amount of Li_2CO_3 and finally calcined at 850 °C for 12 h to obtain the LMNCO-P cathode material.

For the preparation of the Te-doped lithium-rich manganese-based layered cathode material (LMNCO-T), 0.13 g H_6TeO_6 was first dissolved in deionized water, then 2 g as-prepared oxide powder was added into the solution and stirred at 70 °C for 24 h to evaporate the excessive water. The resulting powder was mixed with stoichiometric amount Li_2CO_3 and calcined at 850 °C for 12 h to get the LMNCO-T sample.

The Te-doped lithium-rich manganese-based layered cathode material with a heterogeneous protective layer (LMNCO-TH) was synthesized through a wet coating method. 0.15 g $Mg(NO_3)_2 \bullet 6H_2O$ was mixed in 20 mL polyvinyl pyrrolidone (PVP) aqueous solution (0.05 g/mL) with constant stirring at room temperature for 1 h. Whereafter, 1 g LMNCO-T sample was dispersed in the solution under vigorous stirring at 70 °C for 0.5 h. Then stoichiometric amount $NH_4H_2PO_4$ was added into the above suspension. After stirring for another 5 h, the mixture was filtered and dried at 110 °C, and then calcinated at 450 °C for 6 h. Additionally, the $Mg_3(PO_4)_2$ coated lithium-rich manganese-based layered cathode material (LMNCO-M) was synthesized through the same wet coating method.

2.2. Materials characterizations

The concentrations of metal elements were determined by inductively coupled plasma optical emission spectroscopy (ICP-OES, Perkin Elmer Optima 7300 DV, PerkinElmer). The morphologies of these composites were analyzed by scanning electron microscopy (SEM, JSM-6100LV, JEOL). The surface area and pore volume of samples were studied by N_2 adsorption/desorption using the Brunauer-Emmett-Teller (BET, Micromeritics ASAP2020) method. The crystal phases were characterized using an X-ray diffractometer (Bruker AXS D8) with Cu Kα radiation at 40 kV and 40 mA, and the X-ray diffraction (XRD) results were collected between 2θ = 10-90° with the step size of 0.02° and duration per step of 1.5 s. The crystal parameters were obtained by full spectra fitting and Rietveld refinement of the XRD data through general structure analysis system (GSAS) software. To gather the detailed structural characterizations and elemental distribution, transmission electron microscopy (TEM, JEOL JEM-2100F) and energy-dispersive X-ray spectroscopy (EDS, Bruker Quantax 200) were carried out. The in-situ XRD data were collected at a scanning speed of 0.04° s^{-1} between 2θ = 10-70°, and the time interval for each scan was set for 180 s to ensure enough time to track the structural evolutions of electrodes during cycling. X-ray photoelectron spectroscopy (XPS, ESCALAB 250Xi, Thermo Fischer) with monochromatic Al Kα radiation (hv = 1486.6 eV) was conducted to analyze the valence states of Ni, Co, Mn, O, Te, Mg, and P. The Raman spectra were recorded on a confocal Raman spectrometer (JASCO NRS1000DT) with an air-cooled He-Ne laser at 632.8 nm wavelength. The synchrotron radiation X-ray absorption fine structure (XAFS) spectroscopy measurements, including X-ray absorption near edge structure (XANES) and extended X-ray absorption fine structure (EXAFS) spectra, were performed at the Soft X-ray Microcharacterization Beamline (SXRMB) at the Canadian Light Source, Saskatchewan, Canada. The Ni, Co, Mn, and Te K-edge XAFS data were collected in fluorescence mode using a Si (111) double-crystal monochromator. Differential scanning calorimetry (DSC) measurement was carried out to monitor the thermostability of samples upon a TA (SDT-Q600) instrument at a heating rate of 10 °C min^{-1}.

2.3. Electrochemical measurements

Electrochemical properties of the materials were evaluated using CR2025 coin cells and pouch cells. The as-obtained cathode materials (LMNCO-P, LMNCO-T, and LMNCO-TH) were first mixed with a binder (polyvinylidene fluoride, PVDF) and conductive additive (acetylene black) with the weight ratio of 8 : 1 : 1 in N-methyl-2-pyrrolidone (NMP) and then casted on aluminum foils. The prepared foils were dried

at 110 °C for 12h under vacuum and then pressed under a pressure of 200 kg cm^2. The coin cells were assembled with lithium metals as anodes and porous polypropylene membranes (Celgard 2325) as separators in a glovebox. For pouch cells, the Si/C anode (Glabat Solid-State Battery Inc.) with an areal capacity of ~3.0 mAh cm^{-2} was used, and the capacity balance of anode to cathode was 1.2. The electrolyte for all cells was lithium hexafluorophosphate ($LiPF_6$, 1 mol L^{-1}) dissolved in a mixture solution of dimethyl carbonate (DMC) and ethylene carbonate (EC) (volume ratio = 1:1). The galvanostatic charge and discharge measurements were carried out on a battery testing system (CT-3008, Neware) at various current rates (1 C = 200 mA g^{-1}) in a cutoff voltage range of 2.0-4.6 V (vs Li^+/Li). For the galvanostatic intermittent titration technique (GITT) test, cells were charged/discharged at 0.05 C for activation and then charged/discharged at 0.1 C for an interval τ of 10 min. Subsequently, the cells were kept in open-circuit voltage (OCV) for 60 min to allow the voltage to relax to the steady-state value E_s. Through an electrochemical workstation (SP-300, Bio-Logic), the electrochemical impedance spectroscopy (EIS) test was carried out. The applied frequency range is 0.1 Hz to 1 MHz, and the amplitude is 10 mV.

3. Results and discussion

Spherical morphology is usually vital to promote the tap density and energy density of the nickel-based cathode materials and lithium-rich manganese-based layered oxides. It can be seen from the SEM images in Fig. 2a-c and **Fig. S1**a-f that LMNCO-P, LMNCO-T, and LMNCO-TH samples represent similar particle size distributions and morphology of sphere-shaped particles with diameters of ~9 μm. Moreover, these particles possess compact aggregates of abundant primary nanoparticles. It can not only provide high tap density but also contain ample space for electrolyte and Li^+ ions to permeate from surface to bulk. Furthermore, the LMNCO-P (**Fig. S1**g) and LMNCO-T (**Fig. S1**h) samples exhibit a similar BET specific surface area of about 8.0 m^2 g^{-1}, while LMNCO-TH (**Fig. S1**i) delivers a slightly high value of 8.3 m^2 g^{-1}. The increase of BET specific surface area for the LMNCO-TH can be ascribed to the $Mg_3(PO_4)_2$ coating layer, as will be demonstrated by high-resolution TEM (HRTEM).

To collect the average structural information of LMNCO-P, LMNCO-T, and LMNCO-TH samples, XRD patterns were conducted, as shown in Fig. 2d. The diffraction peaks of all cathode materials match well with each other. They can be well indexed as rhombohedral $LiTMO_2$ phase with the space group of $R\bar{3}m$ (marked by purple color) except for additional weak diffraction peaks between 20 and 26° (2θ), which mainly belong to monoclinic Li_2MnO_3 component with the space group of C2/m (marked by green color) [41,42]. Moreover, all samples illustrate complete splitting of the (006)/(102) and (018)/(110) peaks, indicating the formation of a typical layered phase [43]. The integrated intensity ratio of the (003)/(104) peaks is usually applied to quantify the degree of cation mixing, and the values of all samples are higher than 1.2, revealing low cation mixing [43,44]. Nevertheless, the $I_{(003)}/I_{(104)}$ of LMNCO-TH sample (in the value of 1.37) is slightly lower than of LMNCO-P (in the value of 1.45) and LMNCO-T (in the value of 1.43) samples, which could be ascribed to the formation of minor cations disordered layer in the LMNCO-TH sample. In addition, A close inspection displays that some weak peaks between 20 and 26° (2θ) of the LMNCO-TH sample can't be assigned to the Li_2MnO_3 phase, and apart from that, there is no other impurity peak can be observed in the XRD patterns for all samples. Thus, the enlarged views of the XRD patterns between 20 and 26° (2θ) are presented in Fig. 2e. The diffraction peaks at 20.8, 21.7, and 24.2° (2θ) belong to (020), (110) and ($\bar{1}$11) planes of Li_2MnO_3 phase [34,44], respectively. However, it should be noted that three weak peaks at 23.2, 24.1, and 25.6° (2θ) can only be observed in the LMNCO-TH sample. After careful analysis, the three reflections are more likely to be assigned to the main diffraction peaks of $Mg_3(PO_4)_2$ (PDF#71-1164), and the weak intensities are presumably attributed to the low crystallinity and content of $Mg_3(PO_4)_2$. Combining the XRD and ICP-OES results (**Table 1**), it can be deduced that the Te was successfully doped into the LMNCO-T and LMNCO-TH samples, and $Mg_3(PO_4)_2$ component was indeed formed in the LMNCO-TH sample. To obtain more accurate crystallographic information, the Rietveld refinements of the XRD data for all samples were performed, as shown in **Fig. S1**j-l, and the lattice parameters of all samples were calculated and listed in **Table S1**. The ratio of R$\bar{3}$mand C2/m phases in each sample remains a similar value (3:2), which is in accordance with the original design. Furthermore, Te^{6+} ions in the TM (3b)

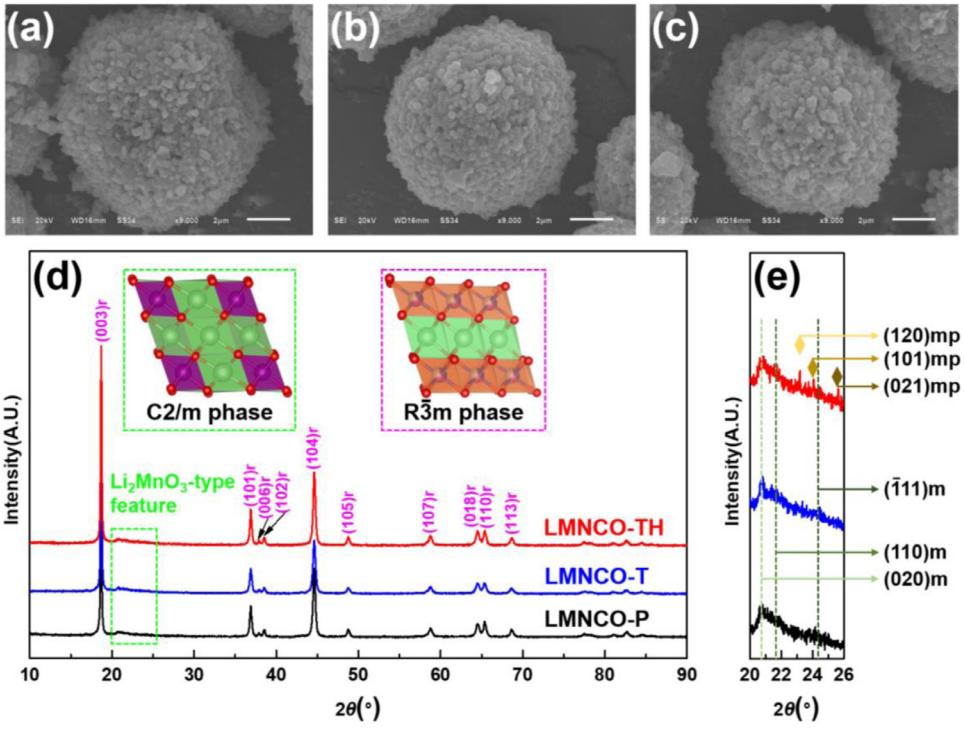

Fig. 2. SEM images of (a) LMNCO-P, (b) LMNCO-T and (c) LMNCO-TH samples; (d) full XRD patterns of LMNCO-P, LMNCO-T and LMNCO-TH samples; (e) enlarged views of the XRD patterns between 20 and 26° (2θ) in (d), showing the difference between these three samples. The insets in (d) are the simulative crystal structures of monoclinic Li_2MnO_3 (space group: C2/m, marked by green square) and rhombohedral $LiTMO_2$ (space group: $R\bar{3}m$, marked by purple square). Scale bars in (a), (b), and (c) are 2 μm.

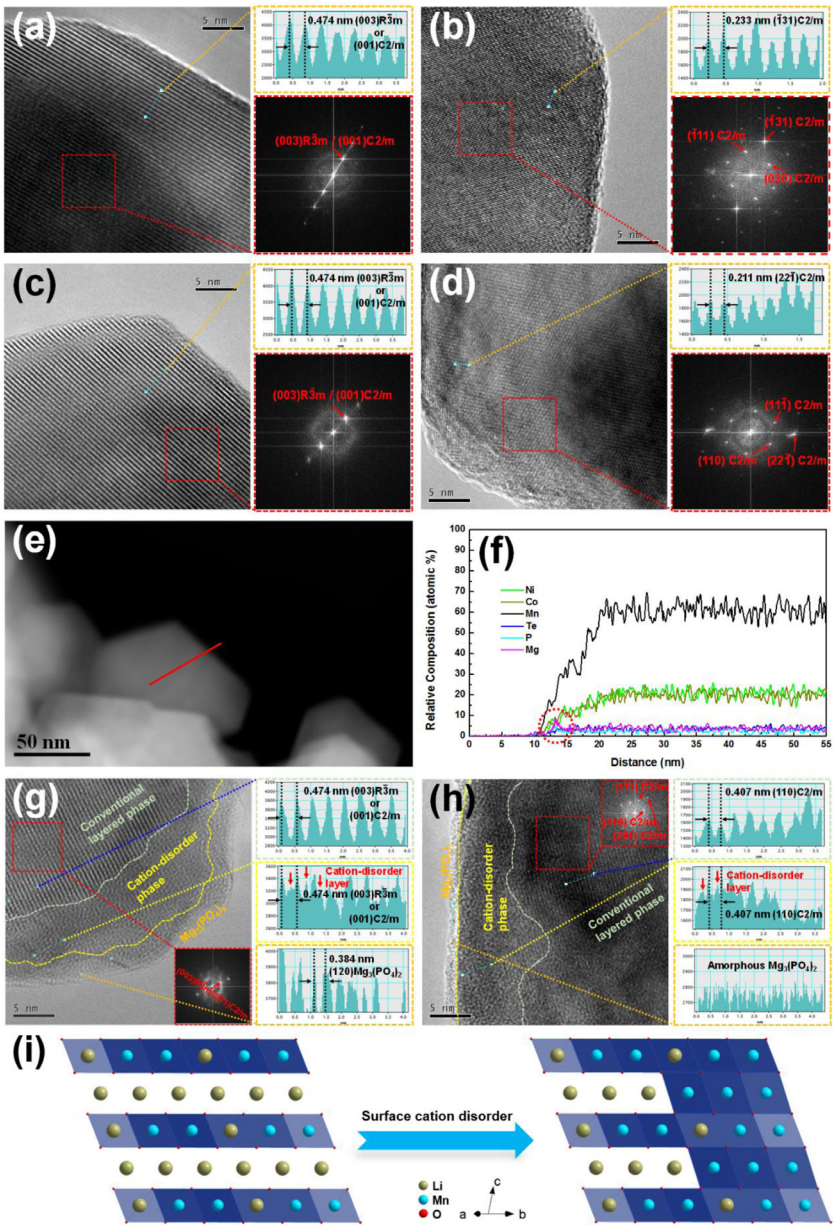

Fig. 3. HRTEM images of (a, b) LMNCO-P and (c, d) LMNCO-T samples; (e) TEM image and (f) EDS line scan profile of a selected primary grain of LMNCO-TH sample; (g, h) HRTEM images of LMNCO-TH sample; (i) simulative crystal structures of conventional monoclinic Li_2MnO_3 and partial cation-disordered Li_2MnO_3. The insets in (a-d, g, h) represent the FFT patterns and signal profiles of the selected regions.

Table 1
Chemical compositions of the LMNCO-P, LMNCO-T, and LMNCO-TH samples determined by ICP-OES.

Samples	Normalized element content (use Ni = 0.200 for all samples)					
	Li	Mn	Ni	Co	Te	Mg
LMNCO-P	1.402	0.599	0.200	0.201	\	\
LMNCO-T	1.399	0.597	0.200	0.198	0.021	\
LMNCO-TH	1.397	0.598	0.200	0.199	0.019	0.027

site of the R$\bar{3}$m phase and Mn (4g) sites of the C2/m phase were constrained for the Rietveld refinement of LMNCO-T and LMNCO-TH samples. The results manifest that the Te^{6+} ions are highly possible to occupy the TM (3b) site. In addition, an obviously increased lattice parameter of R$\bar{3}$m phase can be observed in each modified sample compared with the pristine sample, which may be connected with the increased proportion of TM ions with lower valence and larger ionic radius in the modified samples, as will be demonstrated by XPS examination.

To investigate detailedly the microstructure of the as-obtained cathode materials, TEM and HRTEM were conducted on the LMNCO-P, LMNCO-T, and LMNCO-TH samples, as shown in Fig. 3. The HRTEM image and corresponding signal profile of the selected region (green line) of LMNCO-P sample (Fig. 3a) give clear lattice fringes with an interplanar spacing of 0.474 nm, corresponding to the combination of (003) plane of rhombohedral $LiTMO_2$ structure and (001) plane of monoclinic Li_2MnO_3 structure. [45] The fast Fourier transform (FFT) pattern taken from the selected area (marked by the red square) of HRTEM image (Fig. 3a) can further confirm the above speculation. Furthermore, the analysis of the HRTEM image of the LMNCO-P sample (Fig. 3b) manifestly exhibits a set of lattice fringes that can be indexed to ($\bar{1}$31), ($\bar{1}$11), and (020) planes of monoclinic Li_2MnO_3 structure [19,45,46]. Also, two types of lattice fringes can be observed in Fig. 3c and d, which refer to composite layered structure (the combination of rhombohedral $LiTMO_2$ and monoclinic Li_2MnO_3 phases) and pure monoclinic Li_2MnO_3 phase structure within LMNCO-T sample, respectively. Accordingly, the TM-TM-TM arrangement of the rhombohedral $LiTMO_2$ phase and Li-TM-TM arrangement of the monoclinic Li_2MnO_3 phase coexisted in LMNCO-P

and LMNCO-T sample, and these two samples feature a well-ordered layered structure without Li/TM cations disordering within the Li layer [12]. For the LMNCO-TH sample, TEM and energy dispersive X-ray spectroscopy (EDS) line scanning (Fig. 3e and f) was first performed to characterize the local homogeneity and atomic composition on the surface of the particles. It can be detected that Ni, Co, Mn, and Te elements are uniformly distributed throughout the primary grains, while the P and Mg elements are highly enriched on the surface of the nanoparticles. To further determine the distinction of phase constitution between surface and bulk of the LMNCO-TH sample, the HRTEM images and corresponding signal profiles of the selected regions (marked by the green line) from bulk to surface of the particles were carefully examined, as illustrated in Fig. 3g and h. The LMNCO-TH sample displays the peculiarity of an ordered layered structure in the bulk region, and a $Mg_3(PO_4)_2$ coating layer with a thickness of 2-4 nm can be obviously observed in the outer layer. Nevertheless, in the subsurface region, some strong peaks between TM and TM layers in the line-scan signal profile can be directly observed, which reveals that the partial TM ions enter into the Li layers, indicating Li/TM cations disordering within the Li layers of rhombohedral $LiTMO_2$ and monoclinic Li_2MnO_3 system. Fig. 3i presents the difference between conventional monoclinic Li_2MnO_3 phase and partial cation-disordered structure, it can be found that the well-ordered Li_2MnO_3 phase delivers long-range ordering of 4Li-O-2TM octahedron, and Li-O-Li configuration can be easily formed in the structure (Fig. 1) [10]. In contrast, 4Li-O-2TM ordered structure can be broken in the Li/TM cations disordered structure due to the formation of the 1Li-O-5TM octahedron, thus decreasing Li-O-Li configuration in the surface region of the LMNCO-TH sample. It was reported that over-oxidation of lattice oxygen and oxygen loss in charged LRMOs cathodes mainly proceed by extracting labile electrons from unhybridized O 2p states sitting in Li-O-Li structure [10,36,47,48]. As a result, the redox activity of surface lattice oxygen is expected to be subdued in the LMNCO-TH sample by introducing the heterogeneous protective layer. In addition, the impact of a heterogeneous protective layer on the Li^+ ion diffusion rate can be minimized due to the appropriate thickness of the heterogeneous protective layer and the harmonious transition between the bulk material and the heterogeneous protective layer [31].

XPS analysis was performed to evaluate the oxidation states of ions in the samples. as illustrated in **Fig. S2**a, the Te signal can be detected in the XPS spectrum of the modified samples (LMNCO-T and LMNCO-TH), and Mg and P signals only appear in the XPS spectrum of the LMNCO-TH sample, which is in accordance with the above ICP-OES and TEM-EDS results. The Ni XPS spectra (**Fig. S2**b) consist of two sets of photoelectron peaks: the peaks at binding energies of ~854.0 and ~861.0 eV are assigned to the Ni $2p_{3/2}$ and corresponding satellite peak, the other two peaks at ~872.0 and 879.0 eV correspond to the Ni $2p_{1/2}$ and related satellite peak. The Ni $2p_{3/2}$ profiles can be fitted with two peaks which are located at 854.3 eV (Ni^{2+}) and 855.6 eV (Ni^{3+}), indicating the coexistence of Ni^{2+} and Ni^{3+} in all samples [49,50]. Nevertheless, the concentration ratio of Ni^{2+} and Ni^{3+} (Ni^{2+}/Ni^{3+}) of the modified samples is higher than that of pristine material. **Fig. S2**c and d present the Co 2p and Mn 2p XPS spectra of all samples, and no shift of peak positions can be detected between pristine and modified cathode materials. Moreover, the dominant peaks of Co $2p_{3/2}$ at 780.0 and Mn $2p_{3/2}$ at 642.5 eV demonstrate that the main chemical valences of Co and Mn are +3 and +4 in all samples [33,34,50]. **Fig. S2**e exhibits Te 3d peaks and the Te $3d_{5/2}$ locates at 576.4 eV, demonstrating that Te ions are at the oxidation state of +6 in the LMNCO-T and LMNCO-TH samples [51]. To further identify the oxidation state of Te ions in the bulk of the materials, the LMNCO-T sample was etched for 5 and 10 min and then analyzed by XPS (**Fig. S2**f). The results manifest that the chemical valence of Te is +6 in both surface and bulk of the modified materials. In addition, the Mg 1s peak at 1302.8 eV (**Fig. S2**g) and P 2p peak at 133.3 eV (**Fig. S2**h) can only be detected in LMNCO-TH, and a unique Raman band at ~1000 cm^{-1} can be observed in the spectra of LMNCO-TH sample (**Fig. S3**), which further confirm that the $Mg_3(PO_4)_2$ was

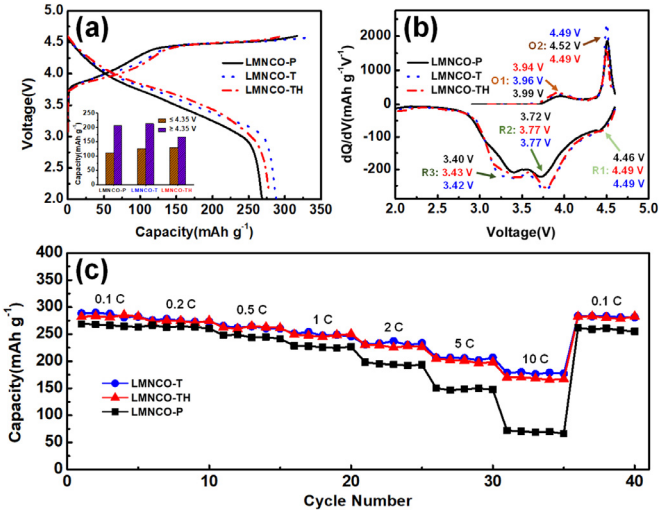

Fig. 4. Comparison of the electrochemical characteristics of the initial cycle at 0.1 C and rate capabilities of LMNCO-P, LMNCO-T, and LMNCO-TH samples: (a) initial cycling curves; (b) differential capacity versus voltage (dQ/dV vs V) profiles of the initial cycle; (c) discharge capacity at various current rates.

successfully coated on the surface of LMNCO-TH sample [52]. To determine the effect of Te^{6+} dopant on the local bonding environment of Ni, Co, and Mn ions in the LMNCO-P and LMNCO-TH samples, the XAFS spectra of several elements were studied in detail. **Fig. S4**a shows Fourier transform magnitudes of the Te K-edge EXAFS spectrum for the LMNCO-TH sample. The first peak at about 1.5 Å contains the information of metal-oxygen interaction for the first coordination shell, and the second peak at about 2.5 Å reveals the metal-metal interaction for the second coordination shell [53]. It is noticeable that the difference between Te and TM (TM = Mn, Ni, Co) K-edge EXAFS spectra is inconspicuous, indicating that the local structure around Te is similar to TM ions [53]. Thus, the Te^{6+} ions prefer to occupy the TM layer, which is in accord with the results of Rietveld refinements of XRD data. Furthermore, The Co, Mn, and Ni K-edge XANES spectra for LMNCO-P and LMNCO-TH samples are presented in **Fig. S4**b-d, and these spectra are sensitive to the local atomic and electronic structure of absorbing atoms. The Co and Mn K-edge XANES spectra do not change after Te doping. However, the absorption edge of the Ni K-edge XANES spectra exhibits a significant change in intensity and shifts to lower energy, corresponding to the variation of the local environment and reduction after Te doping. Accordingly, it can be deduced that the Te^{6+} dopant in the TM layer will mainly affect the local environment of Ni due to the same ionic radius (0.056 nm) between Te^{6+} and Ni^{3+}, and then induce the partial Ni^{3+} ions to be reduced to Ni^{2+} ions, thus may boost TM ions redox capacity.

To explore the electrochemical properties of the as-prepared samples, the half coin cells that assembled with LMNCO-P, LMNCO-T, and LMNCO-TH as cathode materials were characterized. Fig. 4a manifests the initial charging-discharging curves of all samples at 0.1 C between 2.0 and 4.6 V, respectively. Each sample displays a similar characteristic electrochemical behavior of the LRMOs cathodes. In combination with the corresponding differential capacity versus voltage profiles (dQ/dV vs V, Fig. 4b), the initial charging curves can be decomposed into two regions including a short slope line below 4.5 V and a long plateau above 4.5 V. The slope is ascribed to Li^+ ions deintercalation from the rhombohedral $LiTMO_2$ phase accompanied by the oxidation of TM ions (O1 peaks) such as Ni^{2+}/Ni^{3+}, Ni^{3+}/Ni^{4+} and Co^{3+}/Co^{4+} [6], and the capacity of both LMNCO-T and LMNCO-TH is slightly higher than that of LMNCO-P sample at this stage, which is connected with the increased content of Ni^{2+} ions in the modified samples. The long plateau is the signature of the activation of the monoclinic Li_2MnO_3 phase with the irreversible loss of lattice oxygen (O2 peaks) [54]. It's obvious that only the

LMNCO-TH sample possesses distinctly subdued capacity in the plateau region, indicating the decrease of irreversible surface oxygen redox (oxygen loss) by the heterogeneous protective layer with passivated lattice oxygen. During the initial discharging process three reduction peaks appear, and it was reported that the region above 3.6 V referred to hybridized "TM-O reduction" and the region below 3.6 V mainly reflected the "O reduction" [55]. The most significant change between pristine (LMNCO-P) and modified (LMNCO-T and LMNCO-TH) samples is the enhancement in the intensity of reduction peaks at ~3.4 V. The surprising growth of anionic redox could be attributed to the reform of the local environment around lattice oxygen by Te^{6+} ions doping, which can be further determined by the comparison of initial cycling curves (**Fig. S5**a) and differential capacity versus voltage profiles (**Fig. S5**b) between LMNCO-P and LMNCO-M samples. Additionally, compared with the LMNCO-P sample, the electrochemical polarization is reduced for both LMNCO-T and LMNCO-TH samples, suggesting the significantly improved Li^+ ion diffusivity by Te^{6+} ions doping. Hence, the LMNCO-TH delivers a high initial discharge capacity of 282.2 mA h g^{-1} and optimal coulombic efficiency of 95.4% at 0.1 C in the voltage range of 2.0-4.6 V among all samples, as shown in **Table S2**.

The discharge capacities of the as-obtained samples at different current densities from 0.1 C to 10 C (1 C = 200 mA g^{-1}) were also measured. As illustrated in Fig. 4c, at any of the current rates, either LMNCO-T or the LMNCO-TH shows higher discharge capacity than the LMNCO-P sample, indicating that a significant enhancement of rate capability can be obtained through modifying, which is in accordance with the EIS results (**Fig. S5**c). Though the LMNCO-TH sample shows slightly lower discharge capacity than the LMNCO-T sample, which could be attributed to the increase of the Li^+ ion migration barrier in the cation-disordered phase. The discharge capacity of the LMNCO-TH sample can reach 204.7 mA h g^{-1} at 5 C and 168.5 mA h g^{-1} even at 10 C, corresponding to 72.5% and 59.7% capacity retention rate of those at 0.1 C. Instead, The LMNCO-P sample only yields low discharge capacities of 150.3 mA h g^{-1} at 5C and 71.9 mA h g^{-1} at 10 C, respectively, corresponding to 55.8% and 26.7% capacity retention rate of that at 0.1 C. After the high-rate ability test, only the LMNCO-TH sample can almost reach its initial discharge capacity once the current rate restores to 0.1 C, which further confirms the high structural stability of the LMNCO-TH sample. Additionally, the improvement of rate capability is inconspicuous for the LMNCO-M sample (**Fig. S5**d), therefore the enhancement

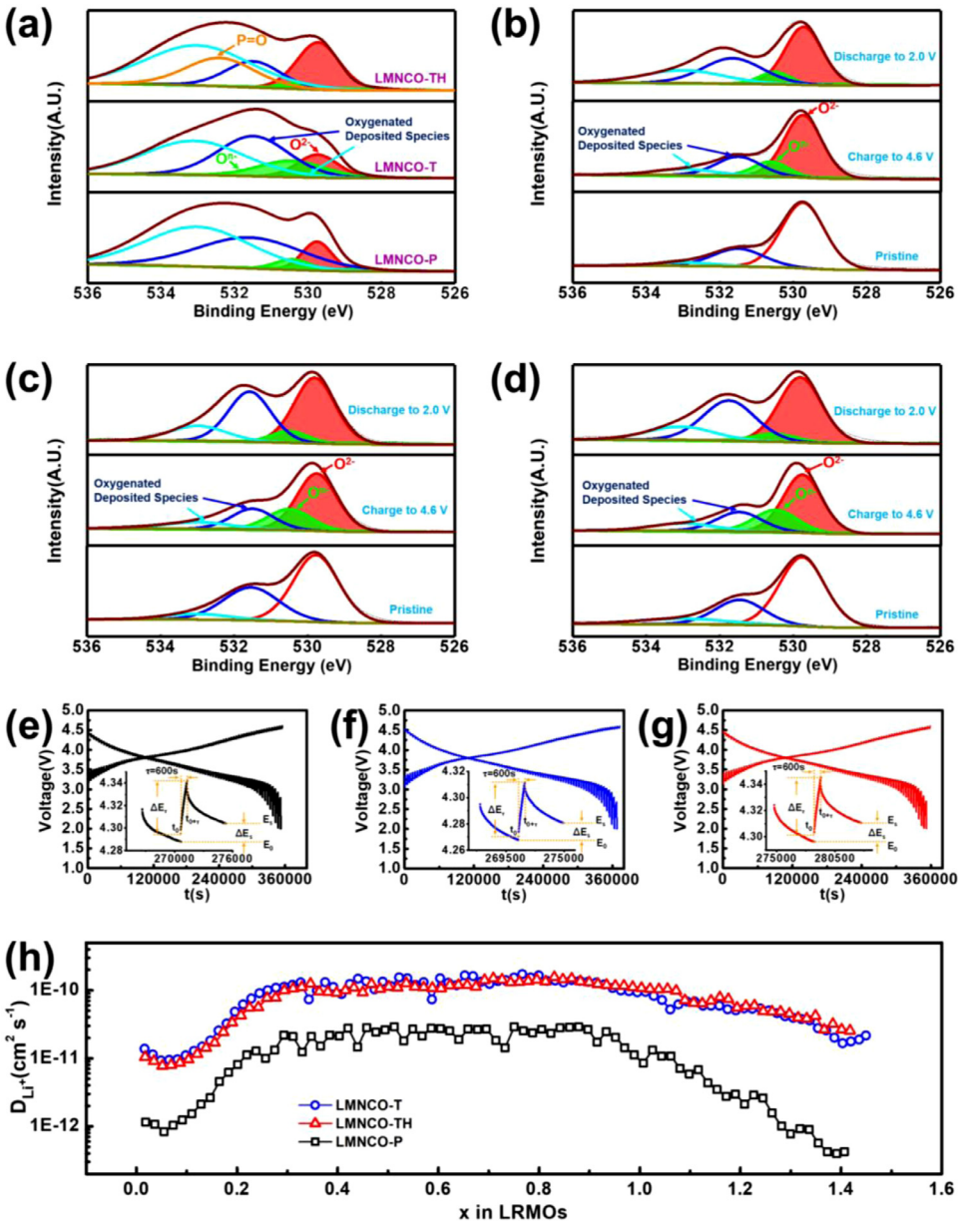

Fig. 5. (a) XPS spectra of O 1s for the LMNCO-P, LMNCO-T, and LMNCO-TH samples after charging to 4.6 V; XPS spectra of O 1s under different charge-discharge states for the etched (b) LMNCO-P, (c) LMNCO-T, and (d) LMNCO-TH samples; (e-g) galvanostatic intermittent titration technique (GITT) curves and (h) Li^+ ion diffusion coefficient ($D_{Li}{}^+$) versus degree of delithiation (x) profiles. The insets in (e-g) are the selected t versus V profiles of single GITT titrations.

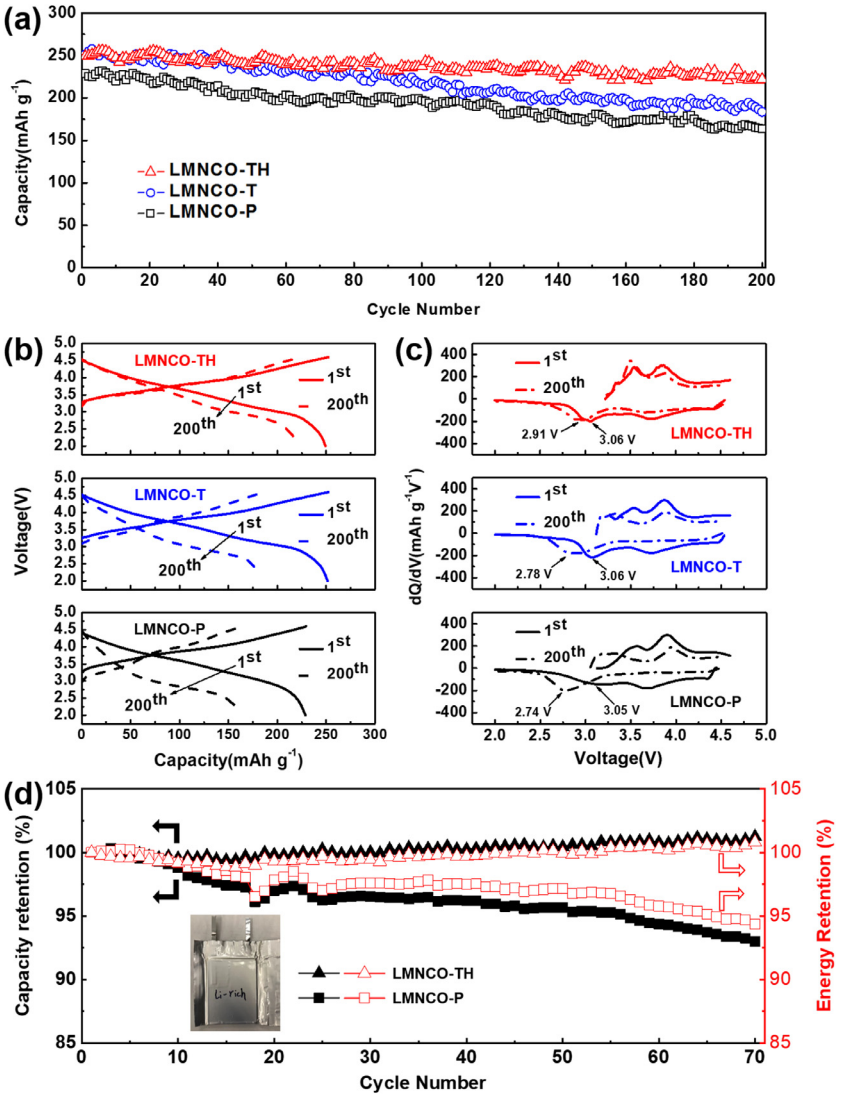

Fig. 6. Comparison of the cycling performance of LMNCO-P, LMNCO-T, and LMNCO-TH samples within 2.0-4.6 V at 1C: (a) variation in discharge capacity versus cycle number; (b) charge and discharge curves of selected cycles; (c) differential capacity versus voltage (dQ/dV vs V) profiles in (b). (d) The cycling retention of discharge capacity and energy density of LMNCO-P and LMNCO-TH samples in pouch full-cells with commercial Si/C anodes within 1.9-4.5 V at 0.5 C.

of the rate capability of LMNCO-T and LMNCO-TH samples could be mainly related to the Te^{6+} ions doping, while the effect of $Mg_3(PO_4)_2$ coating layer on the bulk Li^+ ion diffusivity is little. Such a favorable rate capability of the modified samples is benefited from the improved bulk redox activity and the Li^+ ion diffusivity, which can be demonstrated by Raman spectra, XAFS, and XPS of the electrodes under different charge-discharge states and GITT examination as shown below.

Fig. S6 displays the ex-situ Raman spectra of the electrodes at various charge/discharge states. It can be found that a new peak at ~850 cm^{-1} emerges and the intensity increases during charging, while gradually disappears with the subsequent discharge process, indicating that O^{n-} species (peroxo-like O-O bond) is prone to form when charged to a high voltage (4.6 V) and disappear after discharged to a low voltage (2.0 V) [8]. More importantly, the peak area of peroxo-like O-O bond in both charged LMNCO-T sample and charged LMNCO-TH sample is much higher than that in the charged LMNCO-P sample, suggesting the high oxygen redox reactivity for the charged LMNCO-T and LMNCO-TH samples. To explore further the effect of Te^{6+} doing on oxygen redox reactivity, the Fourier transform magnitude of k^3-weighted K-edge EXAFS data of Te for the pristine and charged LMNCO-TH samples were presented in **Fig. S7**. When the cell is charged to 4.6 V, the peak of Te-O bonding becomes weak, indicating the significant variation of the length of the Te-O bonds. As oxygen participates in the charge compensation, the two O 2p orbitals along with the Li-O-Li configuration slightly rotate, generating the σ-overlapped O-O dimer. According to Ceder's work [36], the oxygen redox is easier when the oxygen ions are bonded to the non-transition metal ions with fully filled or empty d orbitals (such as Te^{6+} ions). Since these ions coordinate the neighboring O^{2-} ions equally by "pure ionic bonding", it can result in less directional M-O bonds, thus making it easier for the O 2p orbitals to rotate. In brief, the oxygen redox reactivity can be actually enhanced by Te^{6+} doping.

Furthermore, the ex-situ XPS of the electrodes in the different charge-discharge states was conducted, as shown in Fig. 5a-d. The O 1s profiles (Fig. 5a) of charged LMNCO-P and LMNCO-T samples can be resolved to O^{2-} (red line, 529.5 eV), O^{n-} (green line, 530.5 eV), and oxygenated deposited species (blue and cyan line, 531.5 and 533.0 eV) peaks [8,10,33,56]. To fit the O 1s curve of the LMNCO-TH sample, another P=O peak (orange line, 532.5 eV) needs to be added [57]. Comparing the LMNCO-T sample with the LMNCO-P sample, the peak intensity of O^{n-} increase with the introduction of Te^{6+} ions. But after coating with a heterogeneous protective layer, the O^{n-} peak intensity of LMNCO-TH is sharply diminished, indicating passivated surface oxygen, which is in accordance with DSC results (**Fig. S8**). As a result, the above results further reveal that the Te^{6+} ions doping can prompt the formation of nonbonding O^{n-} species when charging to a higher voltage due to the rotatable Te-O bond [36], and thus enhancing the oxygen redox activity. More importantly, the heterogeneous protective layer can availably passivate the surface oxygen activity, which is connected with the

high initial coulombic efficiency and reversible specific capacity, portending that high cycling stability can be obtained. Additionally, to investigate the oxygen activation in the bulk, all samples under different charge-discharge states were etched for 10 min, and then were analyzed by XPS, as illustrated in Fig. 5b-d. The charged LMNCO-T sample possesses a higher proportion of nonbonding O^{n-} species than the charged LMNCO-P sample in the bulk lattice, indicating that Te^{6+} doping can indubitably enhance oxygen redox activity. Also, the charged LMNCO-TH sample possesses a similar proportion of bulk nonbonding O^{n-} species with the charged LMNCO-T sample, which demonstrates that the heterogeneous protective layer does not affect the oxygen redox activity of bulk lattice oxygen. It is worth noting that the nonbonding O^{n-} species still exist when discharged to 2.0 V, and this incomplete reduction of O^{n-} species suggests the sluggish kinetics of oxygen redox [6]. Interestingly, the proportions of nonbonding O^{n-} species of the discharged LMNCO-T and LMNCO-TH samples are significantly lower than that of the discharged LMNCO-P sample. Thus the higher oxygen redox kinetics can be obtained by Te^{6+} doping.

To illustrate the effect of the variation of oxygen redox reactivity and local environment of TM ions by Te^{6+} doing on the Li^+ ion diffusion kinetics, a GITT test was conducted. Fig. 5e-g manifests the GITT curves of all samples, and the corresponding t versus V profiles of GITT single titrations are inserted at the bottom of each picture. The Li^+ ion diffusion coefficient ($D_{Li}{}^+$) can be calculated based on the equation (1) as follows [34]:

$$D_{Li^+} = \frac{4}{\pi}\left(I_0\frac{V_m}{FS}\right)^2\left(\frac{dE/dx}{dE/dt^{1/2}}\right)^2, t << \frac{L^2}{D_{Li^+}} \quad (1)$$

where I_0 is assigned to the current, V_m represents the molar volume, F is equivalent to the Faraday constant, S refers to the surface area of the positive electrode, and L manifests the Li^+ ion diffusion length.

As shown in Fig. 5h, the calculated $D_{Li}{}^+$ values of the modified samples in any degree of delithiation are larger than that of the pristine sample. As we know, Li^+ ions generally diffused by hopping-diffusion in the layered cathode materials [20,58]. The $D_{Li}{}^+$ value develops along with the delithiated depth (x) due to the variation of the Li^+ ion diffusion barrier, which is connected with the activation energy of hopping and Li slab space [58]. It was reported that the Li jump pathways contained oxygen dumbbell hopping (ODH) and tetrahedral site hopping (TSH), and the TSH dominated the Li hopping mechanism [58]. For the TSH pathway, the energy barrier near the Ni^{2+} site is much lower than that near the Ni^{3+} site [58], suggesting that the fast Li^+ ion diffusivities in the LMNCO-T and LMNCO-TH samples benefit from the increased content of Ni^{2+} ions. Furthermore, the Te^{6+} dopant can increase the lattice parameter of LRMOs, thereby expanding the interslab spacing and promoting Li^+ migration. More importantly, for the LMNCO-P sample, a sharp drop of $D_{Li}{}^+$ can be clearly observed at the end of delithiation, which is associated with the sluggish oxygen redox at the high charge voltage [6]. By comparison, the $D_{Li}{}^+$ of LMNCO-T and LMNCO-TH samples maintain well at the same stage, which could be attributed to the enhanced oxygen redox activity [45]. In addition, the LMNCO-T and LMNCO-TH samples exhibit a similar Li^+ ion diffusion coefficient, indicating that the heterogeneous protective layer possesses a little negative effect on the Li^+ ion diffusion.

The cycling performance of all samples was evaluated at 1.0 C with a pre-activation at 0.1 C for 3 cycles in the voltage range of 2.0-4.6 V, as shown in Fig. 6a. The initial discharge capacities of the LMNCO-P, LMNCO-T, and LMNCO-TH samples at 1 C are 228.7, 251.3, and 249.2 mA h g^{-1}, respectively. After 200 charging/discharging, the LMNCO-TH sample still exhibits a discharge capacity of 222.2 mA h g^{-1}, corresponding to 89.2% of its initial discharge capacity. Inversely, the discharge capacities of the LMNCO-P and LMNCO-T samples degrade much faster than that of the LMNCO-TH sample and are only 163.7 mA h g^{-1} (71.6% capacity retention) and 183.5 mA h g^{-1} (73.0% capacity retention) in the same cycling period. To investigate the cycling behavior of all samples in-depth, the average discharge voltage, select charge-discharge voltage curves, as well as the corresponding differential capacity profiles, are further compared in **Table S2** and Fig. 6b and c. The LMNCO-P and LMNCO-T samples deliver obvious voltage decay after 200 cycles. On the contrary, the LMNCO-TH sample shows a favorable reproducibility of charge-discharge curves and voltage plateaus, though the voltage fading can't be completely eliminated for the LMNCO-TH sample over the long-term cycling. Moreover, the cycling performance of LMNCO-P and LMNCO-TH pouch full cells is shown in Fig. 6d. It indicates that the discharge capacity and discharge energy density of LMNCO-TH pouch full cell can maintain constant during cycling, while the LMNCO-P full cell delivers obvious decay in both discharge capacity and discharge energy density, demonstrating that heterogeneous protective layer can greatly stabilize the full cell cycling.

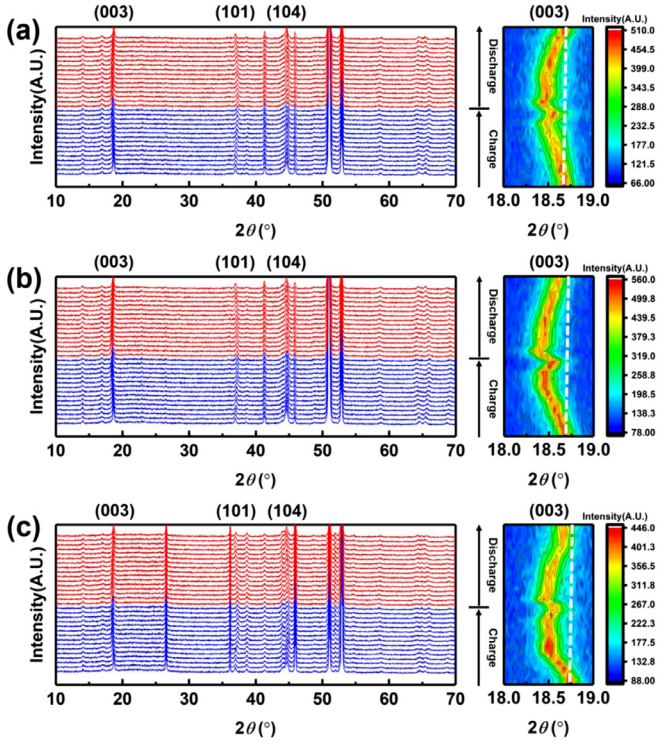

Fig. 7. In-situ XRD patterns and the corresponding enlarged views of the XRD patterns between 18 and 19.5° of the (a) LMNCO-TH, (b)LMNCO-T, and (c) LMNCO-P samples during cycling.

The structural evolutions of the LMNCO-P, LMNCO-T, and LMNCO-TH samples during cycling are further explored. In-situ cells containing the as-obtained cathodes were first fully activated at 0.1 C several times and then cycled at 1 C, and the in-situ XRD patterns during cycling at 1 C were collected. As shown in Fig. 7, the (003) peaks first shift to the low 2θ angle and then to the high 2θ angle along with the Li^+ ions extraction and insertion, which reflects the unit cell expansion and contraction along the c-axis due to the variation of electrostatic repulsion between the oxygen layers [59]. However, the variations of diffraction peak positions for LMNCO-TH are smaller than that of LMNCO-P, LMNCO-T samples, because the uniform distribution of TM ions in the cation-disordered phase was reported to be beneficial to suppress volume expansion/contraction during cycling [60]. Moreover, only the diffraction peak corresponding to the LMNCO-TH sample can entirely recover back to its initial position after discharging to 2.0 V, indicating the excellent reversibility of structural change during cycling. These results also confirm that the LMNCO-TH sample possesses the characteristics of reversible oxygen redox reaction during long-term cycling.

It is generally accepted that the severe capacity and voltage fading are mainly ascribed to the intrinsic structural transformation from layered to deficient spinel-like phase, which occurs firstly on the surface

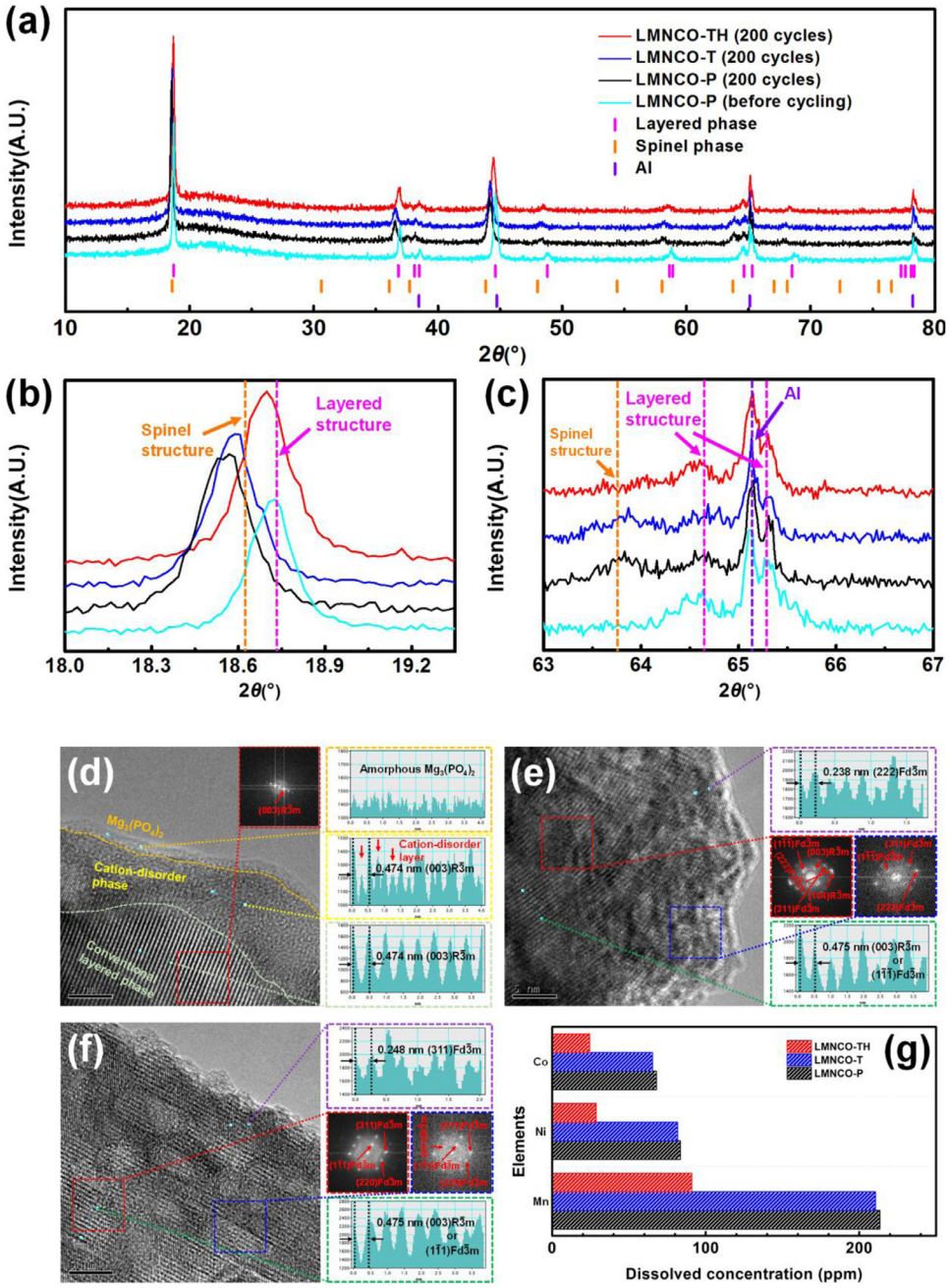

Fig. 8. Evolutions of morphology, crystal structure, and chemical compositions after long-term cycling: (a) comparison of full XRD patterns of all cycled electrodes; enlarged views of the XRD patterns (b) between 18 and 19.3° (2θ) and (c) between 63 and 67° in (a); HRTEM images of (d) LMNCO-TH, (e) LMNCO-T and (f) LMNCO-P samples; (g) concentrations of TM cations in the electrolyte for the samples after cycling. Scale bars in (d), (e), and (f) are 5 nm.

and gradually propagates toward the bulk [14-18]. The structural incompatibility between the original layered lattice and the generated deficient spinel-like phase has been reported to obstruct the complete rehealing of the lattice structures during lithiation on the discharge process, leading to the particles cracking. Furthermore, the newly generated deficient compounds can be easily etched by acidic species and thereafter become fragments after deep cycling [15-17]. Zhang's group observed that numerous Mn^{2+} ion species formed in the fragments, which results in a dramatical decrease in the content of Li^+ ions that can be stored in the LRMOs [17]. Moreover, the voltage at which Li^+ ions intercalate into the deficient spinel-like moieties is about 2.8 V, which is lower than that for Li^+ ions intercalation into the primordial layered structure (>3.0 V) [11,19,20,27]. Thus, the gradual voltage and capacity fading appear, and intensify further along with electrochemical cycling, resulting in a persistent loss of the specific energy. The cycling-induced crack, phase transformation, and TM ion dissolution cause the capacity and voltage fading in the cycling process. Thus the morphology and crystal structure of LMNCO-P, LMNCO-T, and LMNCO-TH samples after 200 cycles at 1 C, as well as concentrations of transition metal cations in the electrolyte after cycling, were characterized by SEM, XRD, HRTEM, XPS and ICP-OES, the results are shown in **Fig. S9**, **Fig. 8** and **Fig. S10**. The SEM results show that the spherical morphology of the cathode for the LMNCO-TH electrode after deep cycling can be well kept. Conversely, the cracking of particles in the cycled electrodes of LMNCO-P and LMNCO-T can be clearly observed. Furthermore, it can be seen from the XRD and HRTEM results that the $LiMn_2O_4$ spinel domains can be observed on the surface and even in the bulk regions of the cycled LMNCO-P and LMNCO-T samples, indicating the severe structure degeneration from the surface to bulk. On the contrary, the layered structure after deep cycling can be maintained well for the LMNCO-TH electrode.

Additionally, it can be found from XPS analysis that the oxidation state of Mn in either cycled LMNCO-P sample or cycled LMNCO-T sample is lower than that in the cycled LMNCO-TH sample, which can further certify that the phase transformation from the layered structure to the $LiMn_2O_4$ spinel can be well inhibited. These results suggest that the heterogeneous protective layer in the LMNCO-TH sample can actually stabilize the LRMOs structure against the severe physical degradation due to its passivated surface lattice oxygen. Furthermore, the dissolved concentration of Co, Ni, and Mn ions in the electrolyte for the LMNCO-TH sample are lowest among all samples, determing the significant effect of heterogeneous protective layer against the acidic species in the electrolyte.

4. Conclusions

In this study, we successfully synthesize the Te-doped lithium-rich manganese-based layered oxides with a heterogeneous protective layer based on a combination of the co-precipitation process and wet coating method. Abundant nonbonding O^{n-} ($n < 2$) species are obtained in the bulk lattice when charged to high voltage (4.6 V) due to the less directional Te-O bond, which can significantly improve anionic redox activity during the cycling process. Meanwhile, the Te^{6+} dopant in the bulk induces partial Ni^{3+} ions to reduce into Ni^{2+} ions, thus maximizing TM ions redox capacity and promoting Li^+ ion transport within the whole particles. The $Mg_3(PO_4)_2$ component with a stable P=O bond can withstand the erosion of acidic species and inhibit TM ions dissolution into the electrolyte. Moreover, the redox activity of surface lattice oxygen is remarkably subdued by introducing the Li/TM cations disordered structure in the subsurface, which prevents the layered-to-spinel transformation and further ensures structural stability. As a result, the unique architecture can significantly boost the initial reversible capacity and rate capability of the material, as well as suppresses the capacity and voltage fading. It reveals that reforming the local environment of oxygen ions in the bulk and surface lattice through facile bulk doping and surface coating is critical for enhancing the electrochemical properties and structural stability of lithium-rich manganese-based layered oxides. Hence, this novel insight may boost the commercialization of lithium-rich manganese-based layered oxides and inspire the development of other layered oxide cathode materials.

Declaration of Competing Interest

The authors declare that they have no known competing financial interests or personal relationships that could have appeared to influence the work reported in this paper.

CRediT authorship contribution statement

Ruizhi Yu: Methodology, Investigation, Data curation, Writing - original draft. **Mohammad Norouzi Banis:** Investigation, Software, Validation. **Changhong Wang:** Investigation, Software, Validation. **Bing Wu:** Investigation, Software. **Yan Huang:** Investigation, Software. **Shuang Cao:** Investigation. **Junjie Li:** Validation. **Sidra Jamil:** Validation. **Xiaoting Lin:** Investigation. **Feipeng Zhao:** Investigation. **Wenhuai Lin:** Investigation. **Baobao Chang:** Investigation. **Xiukang Yang:** Investigation, Validation. **Huan Huang:** Investigation, Validation. **Xianyou Wang:** Project administration, Resources, Supervision, Conceptualization, Validation, Funding acquisition. **Xueliang Sun:** Supervision, Validation.

Acknowledgements

We acknowledge support from the National Natural Science Foundation of China (No. U19A2018) and Key Project of Strategic New Industry of Hunan Province (No. 2019GK2032).

Supplementary materials

Supplementary material associated with this article can be found, in the online version, at doi:10.1016/j.ensm.2021.02.025.

References

[1] P.K. Nayak, E.M. Erickson, F. Schipper, T.R. Penki, N. Munichandraiah, P. Adelhelm, H. Sclar, F. Amalraj, B. Markovsky, D. Aurbach, Review on challenges and recent advances in the electrochemical performance of high capacity Li- and Mn-rich cathode materials for Li-ion Batteries, Adv. Energy Mater. 8 (2018) 1702397.
[2] J. Zheng, S. Myeong, W. Cho, P. Yan, J. Xiao, C. Wang, J. Cho, J.-G. Zhang, Li- and Mn-rich cathode materials: challenges to commercialization, Adv. Energy Mater. 7 (2017) 1601284.
[3] L. Wang, J.-L. Shi, H. Su, G. Li, M. Zubair, Y.-G. Guo, H. Yu, Composite-structure material design for high-energy lithium storage, Small 14 (2018) 1800887.
[4] B. Xiao, X. Sun, Surface and subsurface reactions of lithium transition metal oxide cathode materials: an overview of the fundamental origins and remedying approaches, Adv. Energy Mater. 8 (2018) 1802057.
[5] R.A. House, G.J. Rees, M.A. Pérez-Osorio, J.-J. Marie, E. Boivin, A.W. Robertson, A. Nag, M. Garcia-Fernandez, K.-J. Zhou, P.G. Bruce, First-cycle voltage hysteresis in Li-rich 3d cathodes associated with molecular O_2 trapped in the bulk, Nat. Energy 5 (2020) 777–785.
[6] G. Assat, D. Foix, C. Delacourt, A. Iadecola, R. Dedryvère, J.-M. Tarascon, Fundamental interplay between anionic/cationic redox governing the kinetics and thermodynamics of lithium-rich cathodes, Nat. Commun. 8 (2017) 2219.
[7] B. Li, D. Xia, Anionic redox in rechargeable lithium batteries, Adv. Mater. 29 (2017) 1701054.
[8] X. Li, Y. Qiao, S. Guo, Z. Xu, H. Zhu, X. Zhang, Y. Yuan, P. He, M. Ishida, H. Zhou, Direct visualization of the reversible O^{2-}/O^- redox process in Li-rich cathode materials, Adv. Mater. 30 (2018) 1705197.
[9] S. Zhao, K. Yan, J. Zhang, B. Sun, G. Wang, Reaction mechanisms of layered lithium-rich cathode materials for high-energy lithium-ion batteries, Angew. Chem. Int. Ed. 60 (2021) 2208–2220 DOI:.
[10] G. Assat, J.-M. Tarascon, Fundamental understanding and practical challenges of anionic redox activity in Li-ion batteries, Nat. Energy 3 (2018) 373–386.
[11] E. Hu, X. Yu, R. Lin, X. Bi, J. Lu, S. Bak, K.-W. Nam, H.L. Xin, C. Jaye, D.A. Fischer, K. Amine, X.-Q. Yang, Evolution of redox couples in Li- and Mn-rich cathode materials and mitigation of voltage fade by reducing oxygen release, Nat. Energy 3 (2018) 690–698.
[12] S. Myeong, W. Cho, W. Jin, J. Hwang, M. Yoon, Y. Yoo, G. Nam, H. Jang, J.-G. Han, N.-S. Choi, M.G. Kim, J. Cho, Understanding voltage decay in lithium-excess layered cathode materials through oxygen-centred structural arrangement, Nat. Commun. 9 (2018) 3285.
[13] R. Benedek, H. Iddir, Simulation of first-charge oxygen-dimerization and Mn-migration in Li-rich layered oxides $xLi_2MnO_3 \bullet (1-x)LiMO_2$ and implications for voltage fade, J. Phys. Chem. C 121 (2017) 6492–6499.
[14] J.R. Croy, M. Balasubramanian, K.G. Gallagher, A.K. Burrell, Review of the U.S. department of energy's "deep dive" Effort to understand voltage fade in Li- and Mn-rich cathodes, Acc. Chem. Res. 48 (2015) 2813–2821.
[15] B. Xu, C.R. Fell, M. Chic, Y.S. Meng, Identifying surface structural changes in layered Li-excess nickel manganeseoxides in high voltage lithium ion batteries: a joint experimental and theoretical study, Energy Environ. Sci. 4 (2011) 2223–2233.
[16] M. Gu, I. Belharouak, J. Zheng, H. Wu, J. Xiao, A. Genc, K. Amine, S. Thevuthasan, D.R. Baer, J.-G. Zhang, N.D. Browning, J. Liu, C. Wang, Formation of the spinel phase in the layered composite cathode used in Li-ion batteries, ACS Nano 7 (2013) 760–767.
[17] J. Zheng, M. Gu, J. Xiao, P. Zuo, C. Wang, J.-G. Zhang, Corrosion/fragmentation of layered composite cathode and related capacity/voltage fading during cycling process, Nano Lett. 13 (2013) 3824–3830.
[18] D. Mohanty, J. Li, D.P. Abraham, A. Huq, E. Andrew Payzant, D.L. Wood III, C. Daniel, Unraveling the voltage-fade mechanism in high-energy-density lithium-ion batteries: origin of the tetrahedral cations for spinel conversion, Chem. Mater. 26 (2014) 6272–6280.
[19] P.K. Nayak, J. Grinblat, M. Levi, E. Levi, S. Kim, J.W. Choi, D. Aurbach, Al doping for mitigating the capacity fading and voltage decay of layered Li and Mn-rich cathodes for Li-ion batteries, Adv. Energy Mater. 6 (2016) 1502398.
[20] W.K. Pang, H.-F. Lin, V.K. Peterson, C.-Z. Lu, C.-E. Liu, S.-C. Liao, J.-M. Chen, Effects of fluorine and chromium doping on the performance of lithium-rich $Li_{1+x}MO_2$ (M = Ni, Mn, Co) positive electrodes, Chem. Mater. 29 (2017) 10299–10311.
[21] B. Li, J. Wang, Z. Cao, P. Zhang, J. Zhao, The role of SnO_2 surface coating in the electrochemical performance of $Li_{1.2}Mn_{0.54}Co_{0.13}Ni_{0.13}O_2$ cathode materials, J. Power Sources 325 (2016) 84–90.
[22] H. Zhang, T. Yang, Y. Han, D. Song, X. Shi, L. Zhang, L. Bie, Enhanced electrochemical performance of $Li_{1.2}Ni_{0.13}Co_{0.13}Mn_{0.54}O_2$ by surface modification with the fast lithium-ion conductor Li-La-Ti-O, J. Power Sources 364 (2017) 272–279.
[23] J. Song, Y. Wang, Z. Feng, X. Zhang, K. Wang, H. Gu, J. Xie, Investigation on the electrochemical properties and stabilized surface/interface of nano-$AlPO_4$-Coated $Li_{1.15}Ni_{0.17}Co_{0.11}Mn_{0.57}O_2$ as the cathode for lithium-ion batteries, ACS Appl. Mater. Interfaces 10 (2018) 27326–27332.
[24] S. Zhang, H. Gu, T. Tang, W. Du, M. Gao, Y. Liu, D. Jian, H. Pan, In situ encapsulation of the nanoscale Er_2O_3 phase to drastically suppress voltage fading and capacity degradation of a Li- and Mn-rich layered oxide cathode for lithium ion batteries, ACS Appl. Mater. Interfaces 9 (2017) 33863–33875.

[25] J.-C. Zheng, Z. Yang, P.-B. Wang, L.-B. Tang, C.-S. An, Z.-J. He, Multiple linkage modification of lithium-rich layered oxide $Li_{1.2}Mn_{0.54}Ni_{0.13}Co_{0.13}O_2$ for lithium ion battery, ACS Appl. Mater. Interfaces 10 (2018) 31324–31329.
[26] S. Sallard, D. Sheptyakov, C. Villevieille, Improved electrochemical performances of Li-rich nickel cobalt manganese oxide by partial substitution of Li^+ by Mg^{2+}, J. Power Sources 359 (2017) 27–36.
[27] X. Li, K. Zhang, D. Mitlin, Z. Yang, M. Wang, Y. Tang, F. Jiang, Y. Du, J. Zheng, Fundamental insight into Zr modification of Li- and Mn-rich cathodes: combined transmission electron microscopy and electrochemical impedance spectroscopy study, Chem. Mater. 30 (2018) 2566–2573.
[28] J. Huang, H. Liu, T. Hu, Y.S. Meng, J. Luo, Enhancing the electrochemical performance of Li-rich layered oxide $Li_{1.13}Ni_{0.3}Mn_{0.57}O_2$ via WO_3 doping and accompanying spontaneous surface phase formation, J. Power Sources 375 (2018) 21–28.
[29] S.H. Lee, J.-S. Moon, M.-S. Lee, T.-H. Yu, H. Kim, B.M. Park, Enhancing phase stability and kinetics of lithium-rich layered oxide for an ultra-high performing cathode in Li-ion batteries, J. Power Sources 281 (2015) 77–84.
[30] J. Liu, S. Wang, Z. Ding, R. Zhou, Q. Xia, J. Zhang, L. Chen, W. Wei, P. Wang, The effect of boron doping on structure and electrochemical performance of lithium-rich layered oxide materials, ACS Appl. Mater. Interfaces 8 (2016) 18008–18017.
[31] F. Ding, J. Li, F. Deng, G. Xu, Y. Liu, K. Yang, F. Kang, Surface heterostructure induced by $PrPO_4$ modification in $Li_{1.2}[Mn_{0.54}Ni_{0.13}Co_{0.13}]O_2$ cathode material for high-performance lithium-ion batteries with mitigating voltage decay, ACS Appl. Mater. Interfaces 9 (2017) 27936–27945.
[32] Z. Zhu, R. Gao, I. Waluyo, Y. Dong, A. Hunt, J. Lee, J. Li, Stabilized Co-free Li-rich oxide cathode particles with an artificial surface prereconstruction, Adv. Energy Mater. 10 (2020) 2001120.
[33] S. Zhao, B. Sun, K. Yan, J. Zhang, C. Wang, G. Wang, Aegis of lithium-rich cathode materials via heterostructured $LiAlF_4$ coating for high-performance lithium-ion batteries, ACS Appl. Mater. Interfaces 10 (2018) 33260–33268.
[34] R. Yu, Z. Zhang, S. Jamil, J. Chen, X. Zhang, X. Wang, Z. Yang, H. Shu, X. Yang, Effects of nanofiber architecture and antimony doping on the performance of lithium-rich layered oxides: enhancing lithium diffusivity and lattice oxygen stability, ACS Appl. Mater. Interfaces 10 (2018) 16561–16571.
[35] S. Liu, Z. Liu, X. Shen, W. Li, Y. Gao, M.N. Banis, M. Li, K. Chen, L. Zhu, R. Yu, Z. Wang, X. Sun, G. Lu, Q. Kong, X. Bai, L. Chen, Surface doping to enhance structural integrity and performance of Li-rich layered oxide, Adv. Energy Mater. 8 (2018) 1802105.
[36] D.-H. Seo, J. Lee, A. Urban, R. Malik, S. Kang, G. Ceder, The structural and chemical origin of the oxygen redox activity in layered and cation-disordered Li-excess cathode materials, Nat. Chem. 8 (2016) 692–697.
[37] M. Xu, L. Fei, W. Lu, Z. Chen, T. Li, Y. Liu, G. Gao, Y. Lai, Z. Zhang, P. Wang, H. Huang, Engineering hetero-epitaxial nanostructures with aligned Li-ion channels in Li-rich layered oxides for high-performance cathode application, Nano Energy 35 (2017) 271–280.
[38] J. Lee, D.A. Kitchaev, D.-H. Kwon, C.-W. Lee, J.K. Papp, Y.-S. Liu, Z. Lun, R.J. Clément, T. Shi, B.D. McCloskey, J. Guo, M. Balasubramanian, G. Ceder, Reversible Mn^{2+}/Mn^{4+} double redox in lithium-excess cathode materials, Nature 556 (2018) 185–190.
[39] S. Chen, T. He, Y. Su, Y. Lu, L. Bao, L. Chen, Q. Zhang, J. Wang, R. Chen, F. Wu, Ni-rich $LiNi_{0.8}Co_{0.1}Mn_{0.1}O_2$ oxide coated by dual-conductive layers as high performance cathode material for lithium-ion batteries, ACS Appl. Mater. Interfaces 9 (2017) 29732–29743.
[40] Z. Chen, G.-T. Kim, D. Bresser, T. Diemant, J. Asenbauer, S. Jeong, M. Copley, R.J. Behm, J. Lin, Z. Shen, S. Passerini, $MnPO_4$-coated $Li(Ni_{0.4}Co_{0.2}Mn_{0.4})O_2$ for lithium(-ion) batteries with outstanding cycling stability and enhanced lithiation kinetics, Adv. Energy Mater. 8 (2018) 1801573.
[41] G.Wang R.Yu, M. Liu, X. Zhang, X. Wang, H. Shu, X. Yang, W. Huang, Mitigating voltage and capacity fading of lithium-rich layered cathodes by lanthanum doping, J. Power Sources 335 (2016) 65–75.
[42] M. Xu, L. Fei, W. Zhang, T. Li, W. Lu, N. Zhang, Y. Lai, Z. Zhang, J. Fang, K. Zhang, J. Li, H. Huang, Tailoring anisotropic Li-ion transport tunnels on orthogonally arranged Li-rich layered oxide nanoplates toward high-performance Li-ion batteries, Nano Lett. 17 (2017) 1670–1677.
[43] J.M. Zheng, X.B. Wu, Y. Yang, A comparison of preparation method on the electrochemical performance of cathode material $Li[Li_{0.2}Mn_{0.54}Ni_{0.13}Co_{0.13}]O_2$ for lithium ion battery, Electrochim. Acta 56 (2011) 3071–3078.
[44] G. Singh, R. Thomas, A. Kumar, R.S. Katiyar, A. Manivannan, Electrochemical and structural investigations on ZnO treated 0.5 Li_2MnO_3-0.5$LiMn_{0.5}Ni_{0.5}O_2$ layered composite cathode material for lithium ion battery, J. Electrochem. Soc. 159 (2012) A470–A478.
[45] Q. Li, D. Zhou, L. Zhang, D. Ning, Z. Chen, Z. Xu, R. Gao, X. Liu, D. Xie, G. Schumacher, X. Liu, Tuning anionic redox activity and reversibility for a high-capacity Li-rich Mn-based oxide cathode via an integrated strategy, Adv. Funct. Mater. 29 (2019) 1806706.
[46] F. Fu, J. Tang, Y. Yao, M. Shao, Hollow porous hierarchical-structured $0.5Li_2MnO_3 \bullet 0.5LiMn_{0.4}Co_{0.3}Ni_{0.3}O_2$ as a high-performance cathode material for lithium-ion batteries, ACS Appl. Mater. Interfaces 8 (2016) 25654–25659.
[47] M. Saubanère, E. McCalla, J.-M. Tarascon, M.-L. Doublet, The intriguing question of anionic redox in high-energy density cathodes for Li-ion batteries, Energy Env. Sci. 9 (2016) 984–991.
[48] Y. Xie, M. Saubanère, M.-L. Doublet, Requirements for reversible extra-capacity in Li-rich layered oxides for Li-ion batteries, Energy Env. Sci. 10 (2017) 266–274.
[49] Y. Pei, C.-Y. Xu, Y.-C. Xiao, Q. Chen, B. Huang, B. Li, S. Li, L. Zhen, G. Cao, Phase transition induced synthesis of layered/spinel heterostructure with enhanced electrochemical properties, Adv. Funct. Mater. 27 (2017) 1604349.
[50] W. Liu, X. Li, D. Xiong, Y. Hao, J. Li, H. Kou, B. Yan, D. Li, S. Lu, A. Koo, K. Adair, X. Sun, Significantly improving cycling performance of cathodes in lithium ion batteries: The effect of Al_2O_3 and $LiAlO_2$ coatings on $LiNi_{0.6}Co_{0.2}Mn_{0.2}O_2$, Nano Energy 44 (2018) 111–120.
[51] E. McCalla, A.S. Prakash, E. Berg, M. Saubanère, A.M. Abakumov, D. Foix, B. Klobes, M.-T. Sougrati, G. Rousse, F. Lepoivre, S. Mariyappan, M.-L. Doublet, D. Gonbeau, P. Novak, G. Van Tendeloo, R.P. Hermann, J.-M. Tarascon, Reversible Li-intercalation through oxygen reactivity in Li-rich Li-Fe-Te oxide materials, J. Electrochem. Soc. 162 (2015) A1341–A1351.
[52] W. Liu, P. Oh, X. Liu, S. Myeong, W. Cho, J. Cho, Countering voltage decay and capacity fading of lithium-rich cathode material at 60 °C by hybrid surface protection layers, Adv. Energy Mater. 5 (2015) 1500274.
[53] E.M. Erickson, H. Sclar, F. Schipper, J. Liu, R. Tian, C. Ghanty, L. Burstein, N. Leifer, J. Grinblat, M. Talianker, J.-Y. Shin, J.K. Lampert, B. Markovsky, A.I. Frenkel, D. Aurbach, High-temperature treatment of Li-rich cathode materials with ammonia: improved capacity and mean voltage stability during cycling, Adv. Energy Mater. 7 (2017) 1700708.
[54] P. Xiao, Z.Q. Deng, A. Manthiram, G. Henkelman, Calculations of oxygen stability in lithium-rich layered cathodes, J. Phys. Chem. C 116 (2012) 23201–23204.
[55] W.E. Gent, K. Lim, Y. Liang, Q. Li, T. Barnes, S.-J. Ahn, K.H. Stone, M. McIntire, J. Hong, J.H. Song, Y. Li, A. Mehta, S. Ermon, T. Tyliszczak, D. Kilcoyne, D. Vine, J.-H. Park, S.-K. Doo, M.F. Toney, W. Yang, D. Prendergast, W.C. Chueh, Coupling between oxygen redox and cation migration explains unusual electrochemistry in lithium-rich layered oxides, Nat. Commun. 8 (2017) 2091.
[56] P.E. Pearce, A.J. Perez, G. Rousse, M. Saubanère, D. Batuk, D. Foix, E. McCalla, A.M. Abakumov, G. Van Tendeloo, M.-L. Doublet, J.-M. Tarascon, Evidence for anionic redox activity in a tridimensional-ordered Li-rich positive electrode β-Li_2IrO_3, Nat. Mater. 16 (2017) 580–586.
[57] Q.Q. Qiao, H.Z. Zhang, G.R. Li, S.H. Ye, C.W. Wang, X.P. Gao, Surface modification of Li-rich layered $Li(Li_{0.17}Ni_{0.25}Mn_{0.58})O_2$ oxide with Li–Mn–PO_4 as the cathode for lithium-ion batteries, J. Mater. Chem. A 1 (2013) 5262–5268.
[58] Y. Wei, J. Zheng, S. Cui, X. Song, Y. Su, W. Deng, Z. Wu, X. Wang, W. Wang, M. Rao, Y. Lin, C. Wang, K. Amine, F. Pan, Kinetics tuning of Li-ion diffusion in layered $Li(Ni_xMn_yCo_z)O_2$, J. Am. Chem. Soc. 137 (2015) 8364–8367.
[59] F. Zheng, Q. Deng, W. Zhong, X. Ou, Q. Pan, Y. Liu, X. Xiong, C. Yang, Y. Chen, M. Liu, Fluorine-doped carbon surface modification of Li-rich layered oxide composite cathodes for high performance lithium-ion batteries, ACS Sustainable Chem. Eng. 6 (2018) 16399–16411.
[60] N. Yabuuchi, M. Takeuchi, M. Nakayama, H. Shiiba, M. Ogawa, K. Nakayama, T. Ohta, D. Endo, T. Ozaki, T. Inamasu, K. Sato, S. Komaba, High-capacity electrode materials for rechargeable lithium batteries: Li_3NbO_4-based system with cation-disordered rocksalt structure, PNAS 112 (2015) 7650–7655.